Cancer Diagnostics

Two-Photon In Vivo Imaging with Porous Silicon Nanoparticles

Dokyoung Kim, Jinyoung Kang, Taejun Wang, Hye Gun Ryu, Jonathan M. Zuidema, Jinmyoung Joo, Muwoong Kim, Youngbuhm Huh, Junyang Jung, Kyo Han Ahn, Ki Hean Kim,* and Michael J. Sailor*

A major obstacle in luminescence imaging is the limited penetration of visible light into tissues and interference associated with light scattering and autofluorescence. Near-infrared (NIR) emitters that can also be excited with NIR radiation via two-photon processes can mitigate these factors somewhat because they operate at wavelengths of 650–1000 nm where tissues are more transparent, light scattering is less efficient, and endogenous fluorophores are less likely to absorb. This study presents photolytically stable, NIR photoluminescent, porous silicon nanoparticles with a relatively high two-photon-absorption cross-section and a large emission quantum yield. Their ability to be targeted to tumor tissues in vivo using the iRGD targeting peptide is demonstrated, and the distribution of the nanoparticles with high spatial resolution is visualized.

Photoluminescence (PL) is a versatile tool in chemical, biological, and biomedical science as it enables operationally simple, cost-effective, noninvasive, sensitive, and rapid visualization of organisms at a subcellular level with high resolution.[1–3] Accordingly, various kinds of photoluminescent organic/inorganic labels have been developed for the detection and imaging of analytes, biological systems, diseased tissues, or events.[4–6] For imaging tissues by laser-scanning confocal fluorescence microscopy, typical exogenous luminescent probes offer imaging depths of only a few tens of micrometers, owing to the scattering of light and interference of tissue autofluorescence from intrinsic fluorophores such as riboflavin, flavoproteins, and nicotinamide adenine dinucleotide.[7,8] Two-photon microscopy (TPM) provides a means to increase penetration depth and improve spatial resolution due to the reductions in tissue autofluorescence and scattering associated with the longer wavelengths of both the exciting and emitting photons.[9,10] Thus, TPM has been employed as a minimally invasive tool for numerous short-term and long-term animal studies.[11]

Semiconductor nanocrystals have been harnessed as one or two-photon imaging agents to monitor cellular trafficking,

Prof. D. Kim, M. Kim, Prof. Y. Huh, Prof. J. Jung
Department of Anatomy and Neurobiology
College of Medicine
Kyung Hee University
26 Kyungheedae-Ro, Dongdaemun-Gu, Seoul 02447, Republic of Korea
Prof. D. Kim
Center for Converging Humanities
Kyung Hee University
26 Kyungheedae-Ro, Dongdaemun-Gu, Seoul 02447, Republic of Korea
J. Kang
Department of Nanoengineering
University of California
San Diego, La Jolla, CA 92093-0358, USA
Dr. T. Wang
Division of Integrative Biosciences and Biotechnology
Pohang University of Science and Technology (POSTECH)
77 Cheongam-Ro, Pohang, Gyungbuk 37673, Republic of Korea
H. G. Ryu, Prof. K. H. Ahn
Department of Chemistry
Pohang University of Science and Technology (POSTECH)
77 Cheongam-Ro, Nam-Gu, Pohang, Gyungbuk 37673, Republic of Korea
Dr. J. M. Zuidema
Department of Chemistry and Biochemistry
University of California
San Diego, La Jolla, CA 92093-0358, USA

Prof. J. Joo
Department of Convergence Medicine
University of Ulsan College of Medicine
88 Olympic-ro 43-gil, Songpa-gu, Seoul 05505, Republic of Korea
Prof. J. Joo
Biomedical Engineering Research Center
Asan Institute for Life Science
Asan Medical Center
88 Olympic-ro 43-gil, Songpa-gu, Seoul 05505, Republic of Korea
Prof. K. H. Kim
Division of Integrative Biosciences and Biotechnology
Department of Mechanical Engineering
Pohang University of Science and Technology (POSTECH)
77 Cheongam-Ro, Pohang, Gyungbuk 37673, Republic of Korea
E-mail: kiheankim@postech.ac.kr
Prof. M. J. Sailor
Department of Chemistry and Biochemistry
Department of Nanoengineering
University of California
San Diego, La Jolla, CA 92093-0358, USA
E-mail: msailor@ucsd.edu

**ADVANCED
SCIENCE NEWS**

www.advancedsciencenews.com

**ADVANCED
MATERIALS**

www.advmat.de

tumor microenvironments, and tissue vasculature.[12–16] These materials typically show remarkable photostability compared with organic dyes, and some display sufficient two-photon absorption cross-sections (TPACS, δ) to be of use in two-photon imaging schemes.[17,18] Silicon-based nanocrystals have emerged as promising substitutes for toxic cadmium or lead-based semiconductor nanocrystals;[19–21] the aqueous degradation product of mesoporous silicon is principally $Si(OH)_4$, which is the form of silicon naturally present in tissues of the body.[22] As nanoparticles, the mesoporous form of silicon has been shown to be useful for drug delivery applications, where the 50–80% void volume leads to relatively high capacity for protein, small molecule, or nucleic acid payloads (typical mass loadings in the range of 10–20%).[23–25] The utility of porous silicon nanoparticles (pSiNPs) has been enhanced by the incorporation of tissue-specific targeting elements, which can reduce the overall dose needed to effect productive therapeutic or imaging results in vivo.

One-photon photoluminescence from quantum-confined pSiNPs has been effectively harnessed for bioimaging due to their tissue-penetrating near-infrared (NIR) emission,[26–29] although applications are limited by the short wavelengths needed for efficient excitation (300–450 nm). Imaging silicon nanoparticles (both porous and solid forms) via two-photon excitation has been reported.[30–33] While this has the potential to provide tissue images at greater depths and at higher resolution, no live animal imaging results with intravenously administered silicon nanoparticles have yet been reported, presumably due to their relatively low TPACS and low accumulation in the imaged tissues. Here we demonstrate the utility of pSiNPs for in vivo two-photon imaging by optimizing the pSiNP size to maximize TPACS and by adding a peptide targeting group to selectively accumulate the nanoparticles in tumor tissues.

The pSiNPs were prepared from highly doped p-type single-crystal silicon wafers in aqueous ethanolic electrolytes containing HF (hydrofluoric acid), using an electrochemical perforation etch followed by liftoff, ultrasonic fracture, aging, and isolation as previously described.[34] The perforation etch yields pSi particles with well-controlled particle size and distribution. In the present case, we prepared two size classes for comparison, one of nominal hydrodynamic diameter 60 nm and the other of nominal diameter 230 nm, denoted as 60 nm pSiNPs and 230 nm pSiNPs, respectively (measured by dynamic light scattering (DLS); **Figure 1**a–c, see Figures S1–S3 in the Supporting Information). The ultrasonic fracture process generated a native oxide on the porous Si skeleton (Figure 1a), and this SiO_2 sheath imparted a negative zeta potential (−37.4 ± 3.8 mV; Table S1, Supporting Information) to the nanoparticles. The samples displayed bands in the infrared spectrum consistent with a hydroxylated silicon oxide (Si–O stretching mode at 1020 cm^{-1} and O–H stretching and bending modes at 3300 cm^{-1} and 1640 cm^{-1}, respectively; Figure S3, Supporting Information). The X-ray photoelectron spectra (XPS) were consistent with the existence of a surface oxide layer on the nanoparticles (Figure 1d). Raman spectroscopy (Si lattice mode at 515 cm^{-1}; Figure S3, Supporting Information) and powder X-ray diffraction (XRD) (Figure S3, Supporting Information) analysis showed the pSiNPs retained a crystalline silicon skeleton, although there was a broadening of the peaks associated with crystalline silicon post-ultrasonication. The ultrasonication process also induced a decrease in the total pore volume and average pore diameter as measured by nitrogen absorption–desorption isotherm analysis, consistent with the growth of a SiO_2 sheath on the surface of the pore walls (Figure S4 and Table S2, Supporting Information).

The growth of the SiO_2 sheath activated PL from the nanoparticles (Figure 1e); the increase in the PL signal is attributed to passivation of nonradiative surface defects by the oxide layer. The PL (λ_{ex} = 365 nm) from the 60 nm pSiNPs became detectable after 12 h of ultrasonic fracture, and the intensity of PL maximized at an emission wavelength of 780 nm after ≈48 h of ultrasonication (Figure 1e and Figure S5, Supporting Information). The PL intensity was observed to decrease after 48 h of ultrasonication (Figure S5, Supporting Information), presumably due to degradation and dissolution of the nanoparticles. The radiative recombination of electron–hole pairs confined in crystalline silicon domains is reported to occur at dimensions smaller than 5 nm, approximately the exciton diameter for crystalline silicon.[35] The calculated crystallite size in the skeleton of the 60 nm pSiNPs, determined using the Debye–Scherrer formula from powder XRD data, was 1.5 nm (see Figure S3 and the formula in the Supporting Information). Thus, the nanoparticles can be considered to consist of an ensemble of quantum-confined domains dispersed in the nanoparticle skeleton. Using rhodamine 6G as a standard, the 60 nm pSiNPs showed a quantum yield of 22.3% (Figure S6, Supporting Information), substantially greater than the 9.4% quantum yield of the larger 230 nm pSiNP preparation (Figure S7, Supporting Information).[30] The reason for the greater quantum yield of the smaller pSiNPs is not clear at this time, but it may be due to the presence of fewer quantum-confined domains in a given nanoparticle that can undergo proximal quenching. Alternatively, the smaller nanoparticles may possess a more complete passivating oxide shell.[36] As expected for quantum-confined silicon,[35] the PL emission lifetime for both nanoparticle formulations was on the timescale of microseconds (PL half-life measured at λ_{em} = 780 nm of 106 and 121 μs for 230 nm pSiNPs and 60 nm pSiNPs, respectively; Figure S8 and Table S3, Supporting Information).

We next determined the two-photon transition probability of the pSiNPs using luminescence correlation spectroscopy. We scanned the excitation wavelength range from 750 to 1050 nm and collected emission signals in the wavelength range 560–740 nm to avoid interference of the exciting photons with the pSiNP emission spectrum (Figure 1e). For a process in which excitation results from simultaneous absorption of two photons, the luminescence emission intensity is expected to depend quadratically on average excitation power P_{ex}, or $I_{PL} = (P_{ex})^2 \times \Delta t \times C$, where I_{PL} is the amount of photoluminescence light detected, Δt is the duration of the pulsed excitation, and C represents constants associated with the experimental setup.[37] The measurements were carried out by varying the incident power and recording the corresponding emission intensities for two separate excitation wavelengths, 800 and 850 nm. A log–log plot of emission intensity versus incident power yielded a slope of ≈2.0, as expected for a two-photon absorption process (**Figure 2**a). Under two-photon excitation conditions (λ_{ex} = 850 nm), strong PL was only observed at the focal point of the exciting beam,
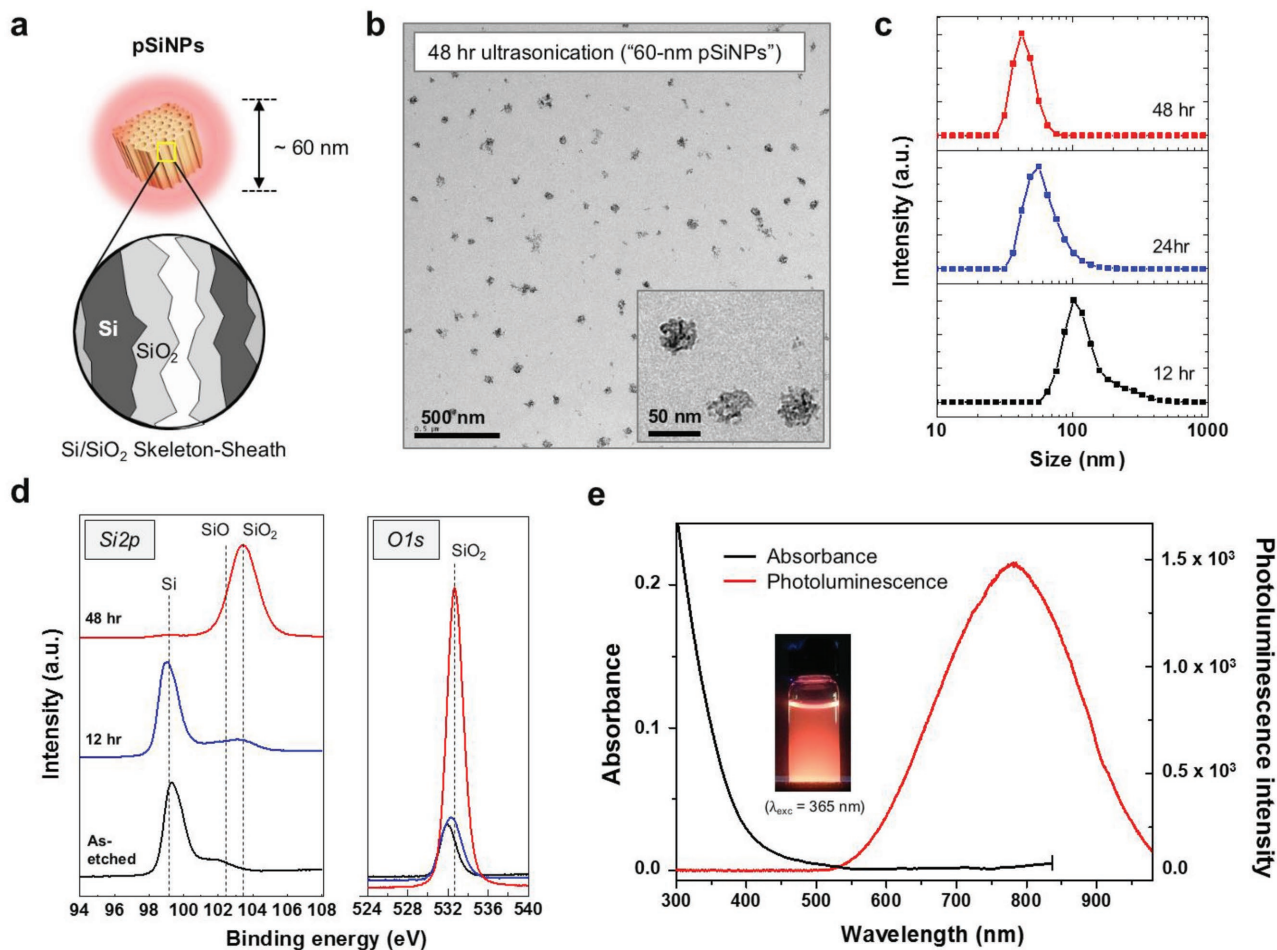
Figure 1. Preparation and characterization of 60 nm pSiNPs. a) Schematic illustration of the skeleton-sheath Si-SiO₂ structure of the porous silicon nanoparticles used in this study. b) Transmission electron microscope (TEM) images of the pSiNPs. These particles were prepared by ultrasonication in deionized water for 48 h. c) Mean hydrodynamic diameter (intensity distribution) of nanoparticles that were ultrasonicated for the indicated time periods, measured by dynamic light scattering (DLS). Particles were isolated at the indicated time points, rinsed, and redispersed in deionized water (DI H₂O) for the measurement. d) X-ray photoelectron spectra (XPS) in the Si2p and O1s regions of nanoparticles that were ultrasonicated for the indicated time periods. "As-etched" refers to the as-etched pSi film, prior to ultrasonication. Assignments: SiO/SiO₂ at 102–104 eV (Si2p) and 532.5 eV (O1s). e) Absorbance and photoluminescence emission spectra of the 60 nm pSiNP formulation. Photoluminescence measured in ethanol using ultraviolet excitation (λ_{ex} = 365 nm). The inset photograph obtained under UV illumination (365 nm).

in contrast to the PL observed along the entire beam path for one-photon excitation (λ_{ex} = 365 nm) (Figure 2b).

The TPACS (δ) of the 60 nm pSiNPs were determined in the excitation range 750–1050 nm using rhodamine 6G as a reference (Figure 2c).[38,39] The maximum TPACS from 60 nm pSiNPs was found to be 5.57 GM (Göeppert-Mayer, 1 GM = 10^{-50} cm⁴ s⁻¹ per photon), and it occurred at an excitation wavelength of λ_{ex} = 800 nm (Figure 2d; for calculation see the Experimental Section). The TPACS of the 60 nm pSiNPs was substantially larger than the corresponding TPACS of the 230 nm pSiNPs at λ_{ex} = 800 nm (5.57 GM vs 1.86 GM for 60 nm and 230 nm pSiNPs, respectively; Figure 2e). For comparison, the maximum TPACS for rhodamine 6G in this wavelength range is 55 GM (at λ_{ex} = 750 nm).[39] However, the 60 nm pSiNPs showed superior photostability compared with the organic dye when subjected to two-photon excitation; negligible emission changes were observed with 20 mW of laser excitation (λ_{ex} = 850 nm) over a period of 60 min, whereas rhodamine

6G showed a 40% loss in intensity under the same conditions (Figure 2f). The resilience demonstrated by the pSiNPs is important for biological imaging applications where longer measurement timescales might be needed and where chromophore photostability can be a limiting factor, such as assaying protein activity, monitoring cellular redox potentials, tracking cell migration, and quantifying accumulation or clearance of probes in tissues.

We next evaluated the nanoparticles as two-photon imaging agents in a tissue-specific targeting application. For this study we chose the tumor-homing peptide iRGD (sequence: CRGD-KGPDC), for two main reasons: 1) it is known to provide selective targeting to (neuropilin-positive) tumor cells;[40] and 2) it has also been shown to be highly effective in targeting pSiNPs to tumors in a mouse xenograft model.[41] Due to their superior two-photon cross-section, these studies used the 60 nm, rather than the 230 nm pSiNP formulation. The peptide was attached to the pSiNPs via a bifunctional poly(ethylene-glycol)

**ADVANCED
SCIENCE NEWS**
www.advancedsciencenews.com

**ADVANCED
MATERIALS**
www.advmat.de
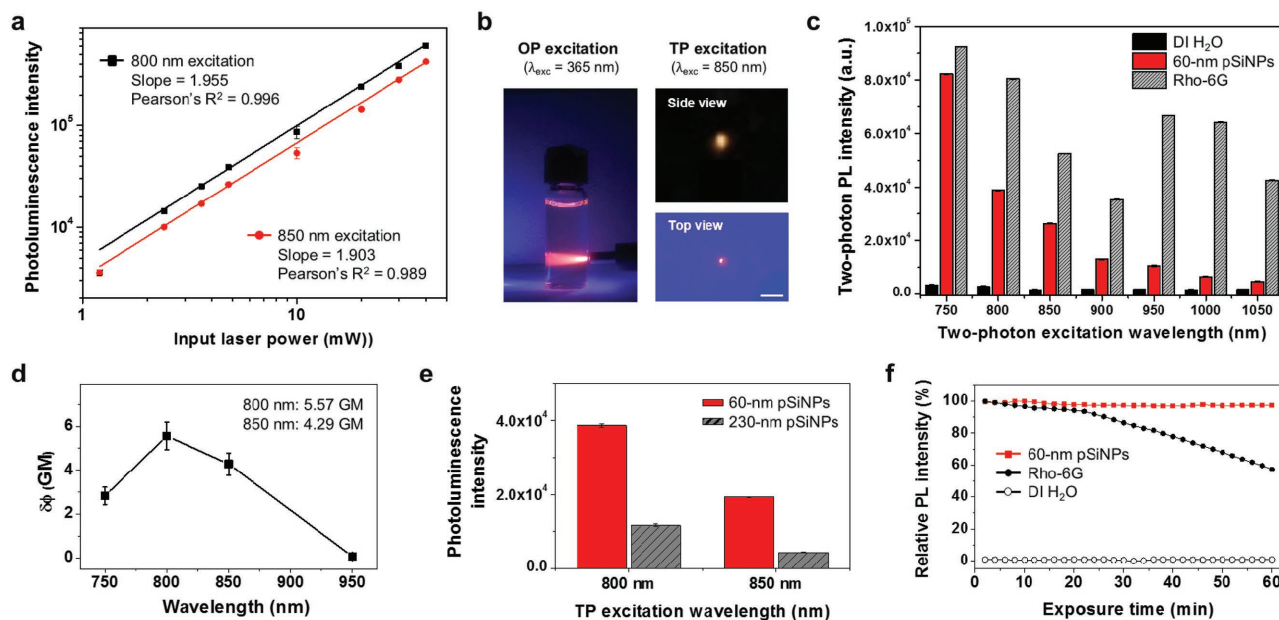
Figure 2. Two-photon photoluminescence characteristics of 60 nm pSiNPs. a) Log–log plot showing laser power dependence of the photoluminescence intensity from 60 nm pSiNPs dispersed in DI H_2O. The pSiNPs were excited using a Ti:sapphire laser emitting at 800 nm (black squares) or 850 nm (red circles), and photoluminescence intensity was collected in the wavelength range 560–740 nm (see the Materials and Methods section in the Supporting Information). b) Photographs showing illumination of a dispersion of 60 nm pSiNPs in DI H_2O using one-photon excitation (λ_{ex} = 365 nm, light comes from right) and focused two-photon excitation (λ_{ex} = 850 nm, power = 100 mW). Scale bar is 1.0 mm. c) Two-photon photoluminescence intensity as a function of λ_{ex} for 60 nm pSiNPs, rhodamine 6G, and DI H_2O control. The pSiNP and rhodamine 6G samples were dissolved in DI H_2O. Samples were excited at the indicated two-photon excitation wavelength and the photoluminescence intensity was quantified in the range 560–740 nm. The same laser power (4.8 mW) was applied for each measurement. d) Two-photon absorption cross-sections (GM) of 60 nm pSiNPs in DI H_2O as a function of excitation wavelength. The error bars represent standard deviation calculated from triplicate measurements (see details in the Supporting Information). e) The two-photon-induced photoluminescence intensity of 60 nm pSiNPs and 230 nm pSiNPs in DI H_2O, measured at excitation wavelengths of 800 and 850 nm, as indicated. The same laser power (4.8 mW) was applied, and the photoluminescence intensity was quantified by integration over the wavelength range 560–740 nm. Standard deviations calculated from triplicate measurements. Each sample contained the same concentration of pSiNPs (1 mg mL^{-1}) or rhodamine 6G (1 μm). f) Comparison of photostability of 60 nm pSiNPs and Rho-6G in DI H_2O under two-photon excitation conditions (λ_{ex} = 850 nm, laser power = 20 mW). Relative photoluminescence intensity was monitored for 60 min at 2 min intervals. The PL signal was collected over the wavelength range 560–740 nm.

(PEG) linker (**Figure 3**a) as follows (Figure S9, Supporting Information): a cysteine thiol on the peptide was coupled to a maleimide group on one end of the PEG linker; the other end of the linker contained a succinimidyl valerate group, which was coupled to a free amine on the pSiNP surface. The free amine groups on the pSiNP surface were previously generated by hydrolytic condensation of 2-aminopropyldimethylethoxysilane (APDMES). The mean hydrodynamic diameter of the resulting construct (named, "60 nm pSiNP-iRGD") increased from the original 60 to 90 nm (mean z-average, intensity based), indicating that the conjugation chemistry placed an ≈15 nm corona around the pSiNP core. The polydispersity index measured by DLS was <0.2, indicating that there was no substantial aggregate formation caused by the conjugation chemistry (Figure S9, Supporting Information). The PL intensity of the pSiNP-iRGD construct under two-photon excitation (λ_{ex} = 850 nm, power = 20 mW) was similar to the pSiNP starting material, and it similarly showed good stability during 60 min of exposure to the excitation source (Figure S9, Supporting Information). The longer-term stability of the nanoparticle construct was assessed in a simple pH 7.4 buffer solution maintained at 37 °C, using one-photon photoluminescence measurements. Under UV excitation (λ_{ex} = 365 nm), the 60 nm pSiNP-iRGD construct lost ≈20% of its PL intensity within 1 h, 50% within 2 h, and PL was near zero after 24 h (Figure S10, Supporting Information).

When incubated with HeLa cells, in vitro cellular TPM images indicated significant uptake of the 60 nm pSiNP-iRGD (Figure 3b and Figure S11, Supporting Information). The nanoparticles localized to the cytosol of the cells and displayed a greater level of cellular uptake relative to untargeted control pSiNPs, consisting of bare pSiNPs (containing just a simple oxide coating) or where the PEG-linker was present but the peptide was replaced with a methoxy group ("pSiNP-mPEG").

We next performed a series of experiments to determine if normal tissues would interfere with the two-photon imaging modality used to detect the pSiNPs. For this evaluation we dissected individual organs (brain, kidney, lung, spleen, and liver) from mice and then incubated them (2 h, 37 °C) in phosphate-buffered saline (PBS) control or in a solution of untargeted, oxide-coated 60 nm pSiNPs (10 mg mL^{-1}). Both one-photon (confocal laser scanning microscope, CLSM) and two-photon images were obtained (Figure S12, Supporting Information). Whereas control tissue samples incubated in buffer only displayed minimal PL signals in the observation channel in either one-photon or two-photon imaging modalities, all organs incubated with pSiNPs displayed strong PL signals (Figure S13,
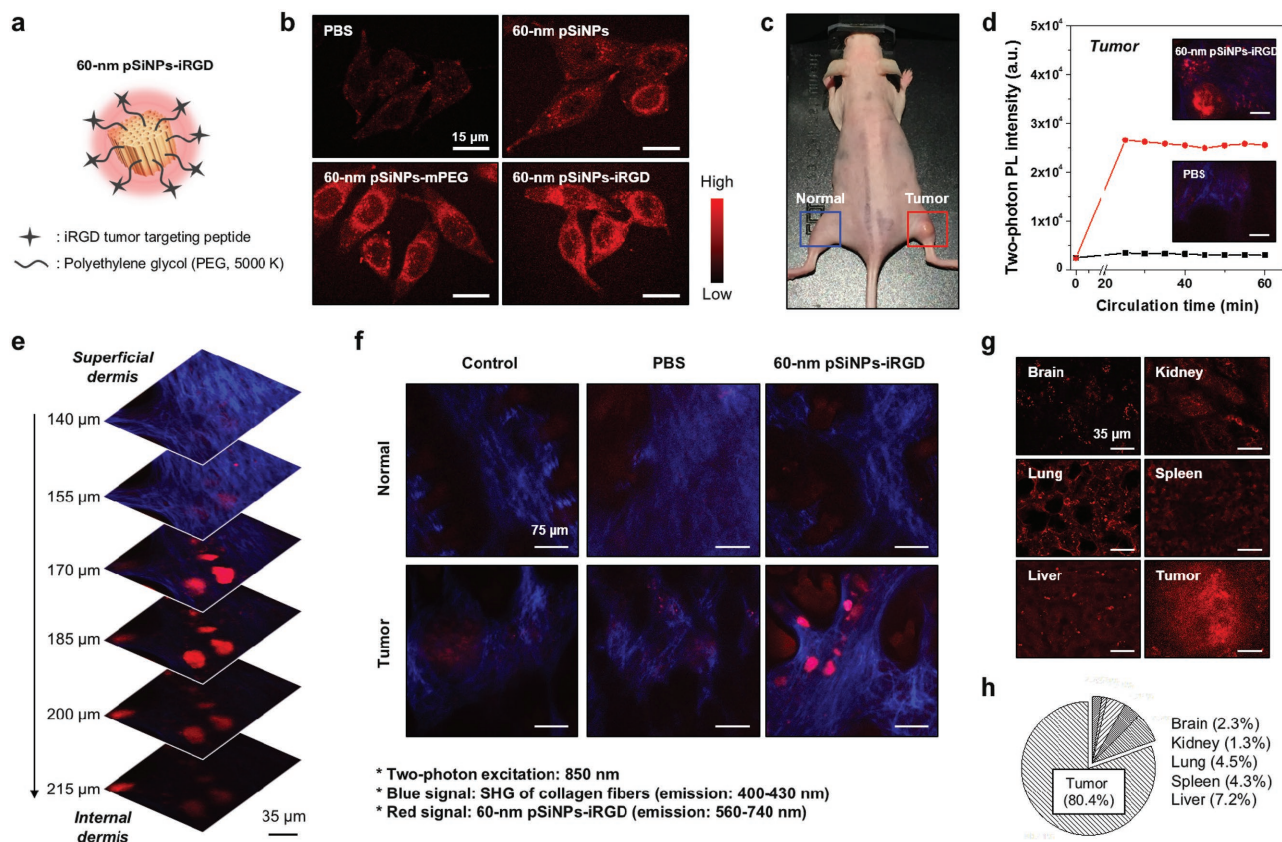
Figure 3. In vitro and in vivo two-photon microscope images of porous Si nanoparticles selectively targeted to tumor tissues. a) Schematic illustration depicting the structure of the 60 nm pSiNP-iRGD construct used (iRGD-specific targeting peptides attached to the pSiNP via 5 kDa PEG linkers, "pSiNP-iRGD"). b) In vitro TPM images of HeLa cells treated with targeted and control 60 nm pSiNPs (20 µg per well) after 30 min incubation at 37 °C. The designation "pSiNP" represents control 60 nm pSiNPs containing only a native oxide surface chemistry. The designation "pSiNP-mPEG" represents control pSiNPs containing the 5 kDa PEG linkers, but each PEG is terminated with a methoxy group instead of the targeting peptide. Laser power 10 mW at the focal plane. c) Photograph of xenograft tumor in the hind limb of a mouse, obtained under ambient light, showing the regions where the in vivo TPM images were collected for normal (blue, left) and tumor (red, right) tissue samples. d) Intensity of signals extracted from TPM images of live animals, obtained in the tumor region for mice injected with 60 nm pSiNP-iRGD (20 mg kg^{-1}, $n = 4$) or with PBS control ($n = 4$), monitored as a function of time postinjection. Time point 0 represents measurements made on animals prior to injection. Laser power ≈50 mW at the focal plane. The intensity data were derived from the TPM images at a depth of 140 µm from the epidermal surface of the animal (along the z-direction), and the inset images correspond to the same depth, obtained 60 min postinjection. Scale bar is 35 µm. e) In vivo TPM images of tumor region acquired at the indicated depths, 60 min postinjection of 60 nm pSiNP-iRGD (20 mg kg^{-1}). Laser power ≈50 mW at the focal plane. The images shown are representative images out of 30 sectional images obtained from depths in the range 100–250 µm. The red and blue signals were collected in the wavelength range 560–740 and 400–430 nm, respectively, corresponding to the pSiNP and the collagen signals, respectively. f) Sections from in vivo TPM images from normal and tumor regions, obtained at a depth of 140–215 µm prior to injection (control) and 60 min postinjection of either PBS or 60 nm pSiNP-iRGD. g) Ex vivo TPM images of organs harvested from animals that were sacrificed 60 min postinjection of 60 nm pSiNP-iRGD (tail-vein injection, 20 mg kg^{-1}). The images shown are representative images obtained at a depth of 45–165 µm. h) Biodistribution of pSiNP-iRGD derived from measured PL intensity from the ex vivo TPM images of panel (g). The percentages represent relative PL intensity from each organ after baseline subtraction; baseline values for each organ were obtained from the PBS-injected controls. All TPM images were obtained with 850 nm excitation, and emission intensity was measured in the wavelength range 560–740 nm.

Supporting Information). The signals were more pronounced in the near-surface region of the organs, though the two-photon images showed stronger signals from the pSiNPs at depths >30 µm into the tissues relative to one-photon CLSM, as can be expected from the greater penetration depth of the two-photon imaging modality (Figures S12 and S13, Supporting Information).

Finally, we evaluated the ability of the targeted pSiNPs to image a near-surface tumor by TPM, using a mouse xenograft tumor model and the 60 nm pSiNPs-iRGD formulation as the imaging agent. Tumor-bearing mice were prepared by subcutaneous inoculation of HeLa cells in the dermal layer (>200 µm depth) of the right hind limb (Figure 3c; see the Materials and Methods section in the Supporting Information). Prior to imaging, the morphological properties of the tumor (Figure 3b, right) and normal (Figure 3b, left) tissue regions were evaluated using optical coherence tomography (OCT).[42,43] The angiographic OCT images revealed randomly distributed, undefined blood vessels in the region surrounding the tumor nodule, and the cross-sectional y–z axis-scanned OCT images provided in-depth information on the tissues: epidermal layer (0–50 µm from skin surface) and dermal layer (below 50 µm) (Figure S14, Supporting Information).

**ADVANCED
SCIENCE NEWS**
www.advancedsciencenews.com

**ADVANCED
MATERIALS**
www.advmat.de

TPM images were then monitored in the region of the tumor nodule. The 60 nm pSiNP-iRGD construct (20 mg kg^{-1}) was administered via intravenous tail-vein injection and monitoring commenced 25 min postinjection, to ensure sufficient time for blood circulation. The data showed substantial two-photon signals in the dermal layers (125–155 μm) compared with the PBS-injected control, indicative of accumulation of the nanoparticles in the tumor region (Figure 3d and Figure S15, Supporting Information). The two-photon emission signal was relatively stable throughout the 1 h monitoring period. The depth dependence of the TPM signal was assessed from the superficial dermal layer (100–150 μm from the skin) to the internal dermal layer (200–250 μm from the surface) at regular intervals (15 μm) in the tumor region, for a period of 60 min post-injection (Figure 3e, and Figure S16 and Movies S1–S2, Supporting Information). The PL emission signal was recorded in two wavelength channels: 400–430 nm, the region where the second harmonic generation (SHG) signal from collagen fibers in the dermal layer appears;[44] and 560–740 nm, the emission window for the 60 nm pSiNP-iRGD construct. Images were acquired under the same two-photon excitation conditions (λ_{ex} = 850 nm, power = 50 mW). The SHG signal from collagen was strong in the superficial dermal layer (blue channel in Figure 3e), and the signal from the nanoparticles was strongest in the zone between 170 and 215 μm from the skin surface (internal dermal layer, red channel in Figure 3e). The z-stacked TPM images of normal and tumor regions at 140–215 μm depths, obtained before injection and after injection of the 60 nm pSiNP-iRGD construct, showed selective accumulation of the nanoparticles. Control injections of PBS showed no significant interference from biological tissues (Figure 3f and Figures S16 and S17, Supporting Information).

The in vivo TPM imaging capability of pSiNPs was compared to the standard two-photon absorber rhodamine 6G. Both probes were injected locally into the dermis near the tumor (at a depth of ≈200 μm from the surface). We chose a localized injection because systemically administered rhodamine 6G shows no organ or tumor specificity. For TPM images of approximately comparable intensity (Figure S18, Supporting Information), the pSiNP dose needed to be much larger (40 μg) relative to rhodamine 6G (20 ng). This reflects the substantially lower two-photon absorption cross-section (Figure 2) and the lower emission quantum yield (Figure S6, Supporting Information) of the pSiNPs relative to rhodamine 6G. Thus although the present in vivo TPM results demonstrate that the combination of NIR emission and NIR two-photon excitation can substantially improve the image quality relative to one-photon, UV excitation, the pSiNPs are substantially weaker than a standard molecular TPM probe. The low toxicity of the silicon system, its ability to carry therapeutic payloads, and its ability to selectively and multivalently target tissues offer substantial advantages to motivate further studies to improve the two-photon cross-section of the silicon nanomaterial.

Distribution and histological studies of the organs collected from the same mice (n = 4) 60 min postinjection were analyzed by ex vivo TPM imaging and hematoxylin/eosin staining. In the TPM images, substantially higher PL intensity was observed in the tumor (hind limb) in comparison with the main organs (brain, kidney, liver, and lung) and PBS-injected control mice

(n = 4) (Figure 3g,h and Figure S19, Supporting Information). The biodistribution data are consistent with the selective homing property previously seen for peptide-targeted pSiNP formulations.[41,45,46] Histopathology showed no significant toxicity in the tissues relative to the control (Figure S20, Supporting Information).

This study represents the first example of two-photon imaging of pSiNPs in live animals, and it demonstrates a potential application in selective tumor imaging. The tumor imaging demonstration presented in this work highlights two advantages of pSiNPs as imaging agents: their multivalent targeting capability for selective tissue homing and their low systemic toxicity. The 60 nm pSiNP formulation showed higher quantum yield (22.3%) and greater two-photon absorption cross-section (5.57 GM at 800 nm, 4.29 GM at 850 nm) relative to larger pSiNPs. While the two-photon absorption cross-section is modest relative to standard molecular two-photon imaging agents such as rhodamine 6G, the photostability under excitation conditions was found to be substantially greater.

Experimental Section

Preparation of pSiNPs (60 nm Size): pSiNPs were prepared by electrochemical etching of highly doped p-type single-crystal silicon wafers in an electrolyte consisting of 3:1 (v:v) 48% HF:absolute ethanol. CAUTION: HF is highly toxic and corrosive and contact with skin should be avoided. Procedures involving HF should always be carried out in a fume hood configured to handle HF and the operator should wear appropriate protective gloves, gown, and face shield. The synthetic procedure is outlined in Figure S1 (Supporting Information). The Si wafers were contacted on the backside with a strip of Al foil. Prior to preparation of the porous layers, the wafer surfaces were cleaned using a sacrificial etch consisting of electrochemical anodization (60 s, 50 mA cm^{-2}) in an electrolyte consisting of 3:1 (v:v) 48% aqueous HF:absolute ethanol, followed by ethanol rinse, then dissolution of the porous film with aqueous KOH (2 M). The wafer was rinsed with water and then with ethanol. A perforation etching waveform[34] was used to prepare the porous layers, which consisted of a current density pulse of 50 mA cm^{-2} of 0.60 s duration, followed by a current density pulse of 400 mA cm^{-2} of 0.363 s duration. This waveform was repeated for 500 cycles, generating a porous nanostructure consisting of ≈60-nm-thick porous silicon layers separated by high porosity ("perforation") layers (Figure S1, Supporting Information). The pSi layer was removed from the silicon substrate by application of a current pulse of 4 mA cm^{-2} for 250 s in a solution containing 1:20 (v:v) aqueous HF:absolute ethanol (lift-off step). The freestanding films (≈63 mg) were fractured by ultrasound in deionized water (DI H$_2$O, 6 mL) for 48 h and aged for 24 h at room temperature (25 °C). The resulting surface-oxidized porous Si-SiO$_2$ frame-sheath nanoparticles were filtered twice through a syringe filter (first through Millipore, Millex syringe filter unit, 220 nm model #SLGP033RS, then a 100 nm model #SLVV033RS) and used without further purification. The concentration of the resulting pSiNP solution was ≈10 mg mL^{-1} in DI H$_2$O (5 mL), yield: 80%. The duration of ultrasonication used in the above description was determined by a systematic optimization study, where nanoparticle size was analyzed as a function of time (12–60 h) of ultrasonication. The average size and size distributions were monitored by DLS and confirmed by transmission electron microscopy (TEM). The nanoparticle size became smaller over time, and the 48 h ultrasonication time was found to yield particles with average hydrodynamic diameters of ≈60 nm.

Grafting of PEG-iRGD to pSiNPs: The 60 nm pSiNPs were separated from the stock solution of pSiNPs prepared above by centrifugation (15 000 rpm, 15 min) using a centrifugal filter (Millipore, MRCF0R100). The as-collected pSiNP pellet (1 mg) was resuspended in ethanol (1 mL),

aminopropyldimethylethoxysilane (APDMES, 20 µL) was added, and the mixture was agitated for 4 h. The aminated nanoparticles (pSiNP-NH$_2$) were then purified three times by centrifugation from ethanol to eliminate unbound APDMES. Then a solution (200 µL) of one of the desired heterofunctional linkers maleimide-PEG-succinimidyl valerate (MAL-PEG-SVA, MW: 5000, 5 mg mL^{-1} in ethanol) or methoxy-PEG-succinimidyl valerate (mPEG-SVA, MW: 5000, 5 mg mL^{-1} in ethanol) was added to the aminated nanoparticles (1 mg in 800 µL) and agitated for 2 h. The resulting PEGylated nanoparticles (pSiNP-PEG or pPSiNP-mPEG) were isolated and purified by centrifugation/resuspension in fresh ethanol three times. For the peptide-conjugated (targeted) formulations, iRGD peptide (sequence CRGDKGPDC, cyclized between the two cysteine residues, 100 µL, 1 mg mL^{-1} in DI H$_2$O) was added to 100 µL of pSiNP-PEG in ethanol, incubated at 4 °C for 4 h, purified three times by centrifugation, dispersed in PBS (pH 7.4, 100 µL), and stored at 4 °C before use.

Photoluminescence Study of pSiNPs: Nanoparticles (either the 60 nm or the 230 nm sizes) were dispersed in ethanol, and photoluminescence intensity was measured using a cooled CCD (charge coupled device) spectrometer (OceanOptics QEPro) using a 365 nm LED (light-emitting diode) light source, a 370 ± 20 nm bandpass filter for excitation, and a 510 nm longpass emission filter. The integrated photoluminescence intensity was obtained in the wavelength range 500–980 nm. Plotted values represent average values ($n = 4$) with error bars representing 1 standard deviation. For the experiments where PL intensity of pSiNPs was monitored as a function of time during aqueous dissolution, particles were dispersed in PBS (pH 7.4, 0.5 mg mL^{-1}) and incubated at 37 °C. The PL intensity was measured at each time point, and particles were transferred to fresh PBS using centrifugation (15 000 rpm, 15 min) through a centrifugal filter (Millipore, MRCF0R100).

Measurement of Two-Photon Cross-Sections of pSiNPs: The two-photon cross-section (δ) was determined using the femtosecond fluorescence measurement technique. Nanoparticles were dispersed in DI H$_2$O and the two-photon-induced luminescence intensity was measured against a rhodamine 6G standard ($QY = 0.95$). 100 µL (1 mg mL^{-1}) of each sample was loaded in single-well glass slides (CITOGLAS, Cat# 2306-0001, Citotest, China) and covered with a glass cover slip. The edges of the cover slip were coated with a transparent nail polish to prevent evaporation of solvent before mounting the slide on the vibration isolation table. The intensities of the two-photon-induced luminescence spectra of the reference and of pSiNPs were measured under the same excitation conditions. The two-photon cross-sections were calculated using the relationship $\delta_s = \delta_r(S_s\Phi_r n_r c_r)/(S_r\Phi_s n_s c_s)$, where the subscripts s and r stand for the sample and reference molecules, respectively; S is the integrated fluorescence intensity at focal plane; Φ is the fluorescence quantum yield; n is the overall fluorescence collection efficiency of the experimental apparatus; c is the number density of the molecules in solution, based on a mass estimation; and δ_r is the two-photon cross-section of the reference sample. The TPACS (GM) was calculated using the relationship GM = $\delta_{max}\Phi$; where Φ is the fluorescence quantum yield of the nanoparticles.[38,39,47]

Preparation of Mouse Xenograft Tumor Model and In Vivo TPM Imaging: All animal experimental procedures were conducted in accordance with institutional guidelines and regulations and approved by the Institutional Animal Care & Use Committee at POSTECH (approval number POSTECH-2015-0030-C1). Hairless mice (SKH1-HrHr, 6 weeks, female) were anesthetized via inhalation of a gas mixture of 1.5% v/v isoflurane (Terrell, Piramal, USA) and medical grade oxygen, and then HeLa cells (5×10^6 cells) were subcutaneously (SC) injected at the right side of the hind limb (dermis layer). TPM imaging was performed 10 d after SC injection of the HeLa cells; tumor growth sufficient for the experiment was confirmed by naked eye and by OCT. The prepared mouse was placed on a custom-made hind limb holder, which was configured to maintain constant temperature and to provide positioning via a motorized *X–Y* translational stage. The 60 nm size pSiNP-iRGD formulation (20 mg kg^{-1}) was intravenously injected via tail vein. In vivo TPM images were obtained with 850 nm excitation (50 mW laser power), and PL intensity was quantified in the wavelength range 560–740 nm. 3D volumetric scanning was performed at 0.4 frames per second and a stepwise increment of 3 µm in the *z*-direction. For the control

experiment, TPM imaging was performed under the same experimental conditions after intravenous tail-vein injection of PBS (200 µL) instead of pSiNPs. Time-lapse images were acquired for 60 min with a time interval of 6 min under constant experimental conditions.

Supporting Information

Supporting Information is available from the Wiley Online Library or from the author.

Conflict of Interest

The authors declare no conflict of interest.

[1] Y. Yang, Q. Zhao, W. Feng, F. Li, *Chem. Rev.* **2013**, *113*, 192.
[2] K. P. Carter, A. M. Young, A. E. Palmer, *Chem. Rev.* **2014**, *114*, 4564.
[3] H. Xiang, J. Cheng, X. Ma, X. Zhou, J. J. Chruma, *Chem. Soc. Rev.* **2013**, *42*, 6128.
[4] E. A. Owens, M. Henary, G. El Fakhri, H. S. Choi, *Acc. Chem. Res.* **2016**, *49*, 1731.
[5] J. V. Jokerst, S. S. Gambhir, *Acc. Chem. Res.* **2011**, *44*, 1050.
[6] P. Zrazhevskiy, M. Sena, X. Gao, *Chem. Soc. Rev.* **2010**, *39*, 4326.
[7] W. R. Zipfel, R. M. Williams, R. Christie, A. Y. Nikitin, B. T. Hyman, W. W. Webb, *Proc. Nat. Acad. Sci. USA* **2003**, *100*, 7075.
[8] S. Huang, A. A. Heikal, W. W. Webb, *Biophys. J.* **2002**, *82*, 2811.
[9] W. R. Zipfel, R. M. Williams, W. W. Webb, *Nat. Biotechnol.* **2003**, *21*, 1369.
[10] C. Xu, W. Zipfel, J. B. Shear, R. M. Williams, W. W. Webb, *Proc. Nat. Acad. Sci. USA* **1996**, *93*, 10763.

[11] K. W. Dunn, T. A. Sutton, *ILAR J.* **2008**, *49*, 66.

[12] J. H. Yu, S.-H. Kwon, Z. Petrášek, O. K. Park, S. W. Jun, K. Shin, M. Choi, Y. I. Park, K. Park, H. B. Na, N. Lee, D. W. Lee, J. H. Kim, P. Schwille, T. Hyeon, *Nat. Mater.* **2013**, *12*, 359.

[13] X. Gao, Y. Cui, R. M. Levenson, L. W. K. Chung, S. Nie, *Nat. Biotechnol.* **2004**, *22*, 969.

[14] H. Wang, T. B. Huff, D. A. Zweifel, W. He, P. S. Low, A. Wei, J.-X. Cheng, *Proc. Nat. Acad. Sci. USA* **2005**, *102*, 15752.

[15] J. Kim, Y. Piao, T. Hyeon, *Chem. Soc. Rev.* **2009**, *38*, 372.

[16] A. Fu, W. Gu, C. Larabell, A. P. Alivisatos, *Curr. Opin. Neurobiol.* **2005**, *15*, 568.

[17] D. R. Larson, W. R. Zipfel, R. M. Williams, S. W. Clark, M. P. Bruchez, F. W. Wise, W. W. Webb, *Science* **2003**, *300*, 1434.

[18] G. D. Scholes, G. Rumbles, *Nat. Mater.* **2006**, *5*, 683.

[19] K. T. Yong, W. C. Law, R. Hu, L. Ye, L. W. Liu, M. T. Swihart, P. N. Prasad, *Chem. Soc. Rev.* **2013**, *42*, 1236.

[20] A. M. Derfus, W. C. W. Chan, S. N. Bhatia, *Nano Lett.* **2004**, *4*, 11.

[21] H. S. Choi, J. V. Frangioni, *Mol. Imaging* **2010**, *9*, 291.

[22] J. R. Henstock, L. T. Canham, S. I. Anderson, *Acta Biomater.* **2015**, *11*, 17.

[23] E. Tasciotti, X. W. Liu, R. Bhavane, K. Plant, A. D. Leonard, B. K. Price, M. M. C. Cheng, P. Decuzzi, J. M. Tour, F. Robertson, M. Ferrari, *Nat. Nanotechnol.* **2008**, *3*, 151.

[24] L. Canham, in *Handbook of Porous Silicon* (Ed: L. Canham), Springer International Publishing, Switzerland **2014**.

[25] J. Salonen, in *Handbook of Porous Silicon* (Ed: L. Canham), Springer International Publishing, Switzerland **2014**, p. 909.

[26] C. M. I. Hessel, E. J. Henderson, J. G. C. Veinot, *Chem. Mater.* **2006**, *18*, 6139.

[27] M. B. Gongalsky, L. A. Osminkina, A. Pereira, A. A. Manankov, A. A. Fedorenko, A. N. Vasiliev, V. V. Solovyev, A. A. Kudryavtsev, M. Sentis, A. V. Kabashin, V. Y. Timoshenko, *Sci. Rep.* **2016**, *6*, 24732.

[28] C. M. Hessel, D. Reid, M. G. Panthani, M. R. Rasch, B. W. Goodfellow, J. W. Wei, H. Fujii, V. Akhavan, B. A. Korgel, *Chem. Mater.* **2012**, *24*, 393.

[29] X. G. Li, Y. Q. He, S. S. Talukdar, M. T. Swihart, *Langmuir* **2003**, *19*, 8490.

[30] J.-H. Park, L. Gu, G. von Maltzahn, E. Ruoslahti, S. N. Bhatia, M. J. Sailor, *Nat. Mater.* **2009**, *8*, 331.

[31] G. S. He, Q. D. Zheng, K. T. Yong, F. Erogbogbo, M. T. Swihart, P. N. Prasad, *Nano Lett.* **2008**, *8*, 2688.

[32] X. S. Xu, S. Yokoyama, *Appl. Phys. Lett.* **2011**, *99*, 251105.

[33] M. Nayfeh, O. Akcakir, J. Therrien, Z. Yamani, N. Barry, W. Yu, E. Gratton, *Appl. Phys. Lett.* **1999**, *75*, 4112.

[34] Z. T. Qin, J. Joo, L. Gu, M. J. Sailor, *Part. Part. Syst. Charact.* **2014**, *31*, 252.

[35] S. Ilya, V. Jan, L. Jan, *Nanotechnology* **2017**, *28*, 072002.

[36] A. Sa'ar, *J. Nanophotonics* **2009**, *3*, 032501.

[37] P. E. Hänninen, M. Schrader, E. Soini, S. W. Hell, *Bioimaging* **1995**, *3*, 70.

[38] A. Fischer, C. Cremer, E. H. K. Stelzer, *Appl. Opt.* **1995**, *34*, 1989.

[39] N. S. Makarov, M. Drobizhev, A. Rebane, *Opt. Express* **2008**, *16*, 4029.

[40] K. N. Sugahara, T. Teesalu, P. P. Karmali, V. R. Kotamraju, L. Agemy, D. R. Greenwald, E. Ruoslahti, *Science* **2010**, *328*, 1031.

[41] J. Joo, X. Liu, V. R. Kotamraju, E. Ruoslahti, Y. Nam, M. J. Sailor, *ACS Nano* **2015**, *9*, 6233.

[42] T. E. de Carlo, A. Romano, N. K. Waheed, J. S. Duker, *Int. J. Retina Vitreous* **2015**, *1*, 5.

[43] B. Kim, T. J. Wang, Q. Li, J. Nam, S. Hwang, E. Chung, S. Kim, K. H. Kim, *J. Biomed. Opt.* **2013**, *18*, 080502.

[44] X. Chen, O. Nadiarynkh, S. Plotnikov, P. J. Campagnola, *Nat. Protoc.* **2012**, *7*, 654.

[45] J. Kang, J. Joo, E. J. Kwon, M. Skalak, S. Hussain, Z.-G. She, E. Ruoslahti, S. N. Bhatia, M. J. Sailor, *Adv. Mater.* **2016**, *28*, 7962.

[46] A. P. Mann, P. Scodeller, S. Hussain, J. Joo, E. Kwon, G. B. Braun, T. Molder, Z.-G. She, V. R. Kotamraju, B. Ranscht, S. Krajewski, T. Teesalu, S. Bhatia, M. J. Sailor, E. Ruoslahti, *Nat. Commun.* **2016**, *7*, 11980.

[47] C. S. Lim, H. J. Kim, J. H. Lee, Y. S. Tian, C. H. Kim, H. M. Kim, T. Joo, B. R. Cho, *ChemBioChem* **2011**, *12*, 392.

1703309 (8 of 8)